

## Article

# Evaluation of Ceramic Properties of Bauxitic Materials from SE of Iberian Range

Domingo Martín <sup>\*</sup>, Adolfo Miras, Antonio Romero-Baena, Isabel Guerrero, Joaquín Delgado , Cinta Barba-Brioso , Paloma Campos  and Patricia Aparicio 

Departamento Cristalografía, Mineralogía y Química Agrícola, Universidad de Sevilla, 41012 Sevilla, Spain; amiras@us.es (A.M.); aromero@us.es (A.R.-B.); iguerrero2@us.es (I.G.); jdelgado15@us.es (J.D.); cbarba@us.es (C.B.-B.); pcampos1@us.es (P.C.); paparicio@us.es (P.A.)

\* Correspondence: dmartin5@us.es; Tel.: +34-954-55-63-20

**Abstract:** The use of aluminum-rich clays and bauxites as refractory materials is common. Upon firing, these materials form mullite crystals in the shape of needles embedded in a siliceous and vitreous matrix, with mullite being responsible for the refractory properties. In this study, bauxite samples for use in refractory applications have been characterized. Chemical analysis revealed that the alumina content varied between 34 and 40%, with silica values generally being high (around 40%), except for one sample (26%). Two samples were found to be the most suitable for use as “refractory clay” refractories. However, high silica or Fe oxide contents can affect mineralogical transformations at high temperatures. Mineralogical analysis confirmed the presence of several minerals in the bauxite materials, including kaolinite, halloysite, anatase, rutile, gibbsite and boehmite. Differential thermal analysis (DTA) showed the decomposition of gibbsite and its partial transformation to boehmite and alumina, and the dehydroxylation of kaolinite, with primary mullite crystallization observed at a high temperature. These findings provide valuable information for the selection and optimization of bauxite materials for refractory applications, considering their chemical composition and mineralogical characteristics.

**Keywords:** bauxitic materials; ceramic properties; refractory materials; clayey ceramic



**Citation:** Martín, D.; Miras, A.; Romero-Baena, A.; Guerrero, I.; Delgado, J.; Barba-Brioso, C.; Campos, P.; Aparicio, P. Evaluation of Ceramic Properties of Bauxitic Materials from SE of Iberian Range. *ChemEngineering* **2024**, *8*, 13. <https://doi.org/10.3390/chemengineering8010013>

Received: 8 November 2023

Revised: 29 November 2023

Accepted: 2 January 2024

Published: 8 January 2024



**Copyright:** © 2024 by the authors. Licensee MDPI, Basel, Switzerland. This article is an open access article distributed under the terms and conditions of the Creative Commons Attribution (CC BY) license (<https://creativecommons.org/licenses/by/4.0/>).

## 1. Introduction

Knowledge about the nature, genesis, properties, and applications of refractory materials is one of the main topics in research and technological developments carried out in the field of ceramic materials [1]. Refractory materials can resist high temperatures (about or above 1500 °C) without experiencing breakage or deformation. A high melting point, mechanical resistance at high temperature and resistance to chemical attack characterizes them. The main applications of refractory materials include refractory bricks for kilns and furnaces, crucibles, thermocouple lining, cements, etc. [2–8].

One of the most important traditional refractory materials is made of aluminum-rich raw clays and bauxites, commonly referred to as “refractory clays”. These include kaolinite clays, bauxite and lateritic clays, which are composed of high alumina and moderate melting components such as alkaline and earth alkaline elements, silica or iron oxide.

Bauxites and lateritic clays are products from the weathering and leaching of a variety of rocks, typically found in tropical or subtropical climates with high precipitation rates [9,10]. The weathering process results in the destruction of the primary silicates in the rocks and the leaching of alkaline and alkaline earth elements, as well as silica, leading to an enrichment in aluminum (Al) and iron (Fe), which are practically insoluble between pH 4 and 10. This results in the formation of clay minerals of the kaolinite type, as well as oxy-hydroxides of iron and aluminum [11]. Typically, these clays contain bauxite minerals such as gibbsite (Al(OH)<sub>3</sub>) and other aluminum oxides (boehmite and diaspor, AlO(OH)),

kaolinite ( $\text{Al}_2\text{Si}_2\text{O}_5(\text{OH})_4$ ) and other minor components [12]. Bauxites can occur in different forms, varying significantly in their physical properties, such as being massive or earthy, pisolitic, nodular, cellular, vermicular, etc. High-quality bauxites are generally light gray, although there are also darker colored bauxites rich in organic matter.

High-quality bauxite deposits with alumina content greater than 47.5% are desirable to produce high alumina bricks. However, the depletion of such high-quality bauxite deposits has led to the increased use of aluminum clays with lower alumina content, down to 40%, as a replacement. While the alumina content is slightly lower in these aluminum clays, they can still be used in the production of refractory materials, albeit with some adjustments in formulation and processing conditions to compensate for the lower alumina content [3]. This allows for the continued use of refractory clays as a viable raw material for refractory production, even with the decrease in high-quality bauxite deposits.

After firing, the structure of this material consists of needle-like mullite crystals in a siliceous and vitreous matrix with some impurities [13–15]. Mullite is responsible for the refractory properties of this material due to its very low thermal expansion coefficient and an excellent thermal shock resistance. However, the use of bauxite as a refractory raw material is dependent on other components [16,17]. Impurities such as iron oxy-hydroxides and titanium oxides decrease the melting point and cause deformation that deteriorates the properties of refractory at high temperatures [16,18]. In silica–aluminum systems, mullite melting starts at 1828 °C, while the presence of iron decreases the melting point down to 1205 °C [18,19]. Alkaline and alkaline earth oxides constitute fluxes, which decreases the melting temperature even at low concentrations [20–22]. Free silica also reduces the refractory properties and the quality of the final product due to its contribution to increased contraction of the refractory [23,24]. Therefore, the quality of natural bauxite for refractory production depends on its mineralogical and chemical characteristics.

In the northeastern part of the Iberian Plate, where the Iberian Range is situated, a seasonal subtropical climate prevailed during the Upper and Lower Cretaceous periods. These climatic conditions were conducive to the formation of clay deposits enriched with kaolinite and illite, as well as bauxites and lateritic clays [25–27]. More precisely, extensive bauxite reservoirs are predominantly distributed along the emerged areas of the region [28].

According to data from the Mining Statistics of Spain (2021) [29], the production of refractory clays has reached values of over 640,000 tons, with approximately 40% of  $\text{Al}_2\text{O}_3$  distributed among a few dozen operations in the study area, and with a capital value close to EUR 35 million.

The objective of this study is to analyze the ceramic properties of selected bauxite samples from the southeastern region of the Iberian Range, specifically the Maestrazgo zone in Spain. This study aims to evaluate the impact of the chemical and mineralogical composition of the bauxite samples on their suitability for use as refractory materials.

## 2. Materials and Methods

Four samples were collected from the Lower Cretaceous karst bauxite deposits outcropping the SE of the Iberian Range (Maestrazgo zone) (Figure 1). The samples, labeled as F2-X, F2-Y and F4-4 (from Fuentespalda, Teruel) and FR-9 (from Fredes, Castellón), were selected for this study. These bauxite deposits are found as small bodies filling karst cavities that have developed in Jurassic limestones [25,30,31] (Figure 2).

The materials were characterized chemically and mineralogically. The chemical composition was determined using X-ray fluorescence (XRF) analysis with a Panalytical AXIOS equipment. The samples were prepared in a glass bead with a sample-to-lithium borate flux ratio of 1/9, using milled and sieved samples passing through a 100  $\mu\text{m}$  sieve.

The mineralogical analysis was conducted using X-ray diffraction (XRD) with a Bruker D8 Advance A25 powder diffractometer equipped with a Linxeye linear detector. The analysis was performed under standard conditions including Cu  $k\alpha$  radiation ( $\lambda = 1.54056 \text{ \AA}$ ), 40 kV and 30 mA, with a scanning range of 3–70° (2 $\theta$ ), a step size 0.015° and time per step of 0.1 s. Divergence slit 0.5°, Ni filter and sample rotation at 30 r.p.m. were used.

The patterns were obtained by the powder method, using a side-loading sampler holder to ensure maximum random orientation. The clay fraction was studied by orientated aggregates of the <math><2\ \mu\text{m}</math> fraction, after air-drying, ethyleneglycol solvation and heating at 550 °C. The patterns were performed between 3 and 40° ( $2\theta$ ), with a divergence slit of 0.1°, and the remaining conditions were identical to those used in the powder samples.

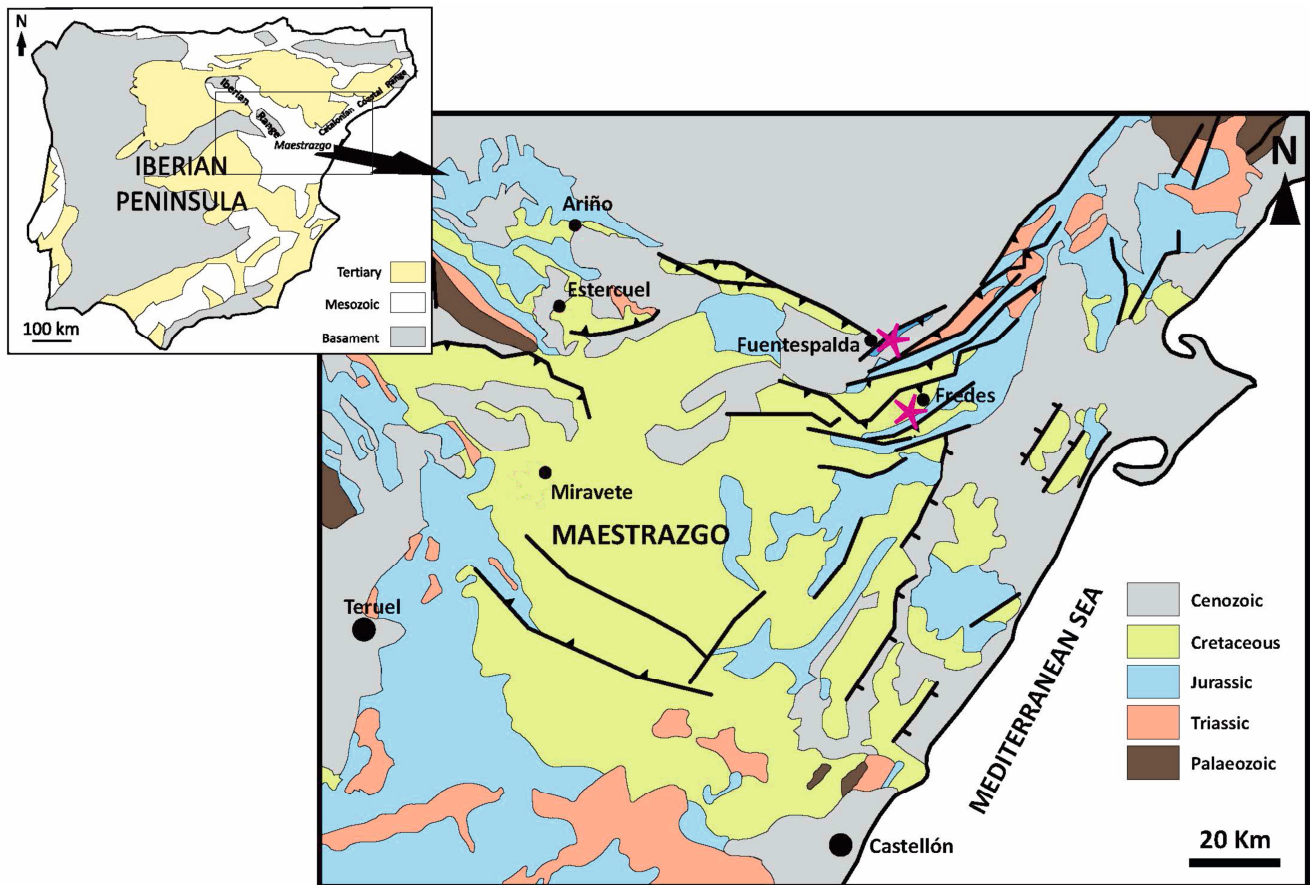


Figure 1. Geological setting and sampling location (with start symbol).

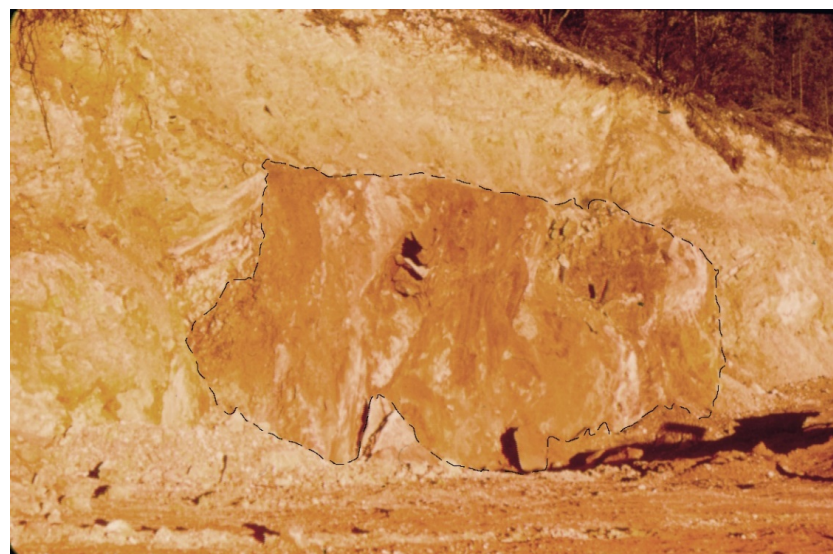


Figure 2. Karstic pocket filled with bauxite materials (Fuentespalda, Teruel).

A semi-quantitative mineralogical analysis was performed using a quantitative mineralogical approach. Diagnostic reflection areas were measured, considering the full width at half maximum (FWHM), and corrected by empirical factors based on the methods proposed by [32–34]. The percentages of the different clay minerals were then calculated from the areas of the diagnostic basal diffraction of the phases in the glycolated clay fraction. The halloysite/kaolinite ratio was determined using the method proposed by Aparicio and collaborators [35], which involves fitting the 002 reflections from kaolin in the pattern.

In addition to XRD, the mineralogical analysis was supplemented with differential thermal and thermogravimetric analysis (DTA/TG). DTA/TG was conducted using a Netzsch STA 409 PC instrument, with a heating rate of  $10\text{ }^{\circ}\text{C min}^{-1}$ , ranging from 30 to  $1200\text{ }^{\circ}\text{C}$ , under  $\text{N}_2$  atmosphere at a flow rate of  $50\text{ mL min}^{-1}$ , and utilizing alumina crucibles.

The structural order of kaolinite was determined using two methods. First, the AGFI index [36,37] was calculated from the XRD powder patterns. Secondly, an evaluation of symmetry was executed concerning the endothermic signal manifesting ca.  $575\text{ }^{\circ}\text{C}$  in the patterns of DTA [38].

The ceramic technological properties were studied using the following methods:

- (a) Observations by tunnel heating microscopy using a Termolab tubular oven, model TA1600 (Termolab, Aveiro, Portugal), with a diameter of 65 mm, capable of reaching temperatures above  $1500\text{ }^{\circ}\text{C}$ . Cylindrical test pieces measuring 5 mm in diameter and 10 mm in length, obtained by dry pressing 0.20 g of the sample at 1 kN, were subjected to a heating curve of  $20\text{ }^{\circ}\text{C min}^{-1}$  up to  $1000\text{ }^{\circ}\text{C}$ , followed by  $10\text{ }^{\circ}\text{C min}^{-1}$  up to  $1500\text{ }^{\circ}\text{C}$  for observation and analysis.
- (b) The evolution of the XRD mineralogical phases during heating was analyzed using an internal standard (15% wt. of zincite, Sigma Aldrich, Steinheim, Germany). The same conditions as for the raw materials were applied. The cylinder samples tested were fired at temperatures of  $1100\text{ }^{\circ}\text{C}$ ,  $1200\text{ }^{\circ}\text{C}$ ,  $1300\text{ }^{\circ}\text{C}$ ,  $1350\text{ }^{\circ}\text{C}$ ,  $1400\text{ }^{\circ}\text{C}$  and  $1450\text{ }^{\circ}\text{C}$  in a programmable high-temperature oven Thermolyne brand, model Type 46120 (Thermolyne-ThermoFisher Scientific, Waltham, MA, USA), in oxidizing atmosphere, with a heating rate of  $2\text{ }^{\circ}\text{C min}^{-1}$  and a soaking time of 2 h. The XRD patterns were obtained and analyzed for mineralogical phase changes during the heating.
- (c) Water absorption and open porosity were determined by Archimedes's immersion technique, following the ASTM C20-00(2022) standard [39]. The samples were immersed in boiling water, and the change in weight was measured to determine water absorption and open porosity. Apparent density was determined using a helium pycnometer (Pentapycnometer 5200e, Quantachrome Instruments, Boynton, FL, USA), which measures the volume of gas displaced by the sample, allowing for the calculation of apparent density. Linear shrinkage was determined by measuring the change in sample length after drying at  $110\text{ }^{\circ}\text{C}$  and after firing at different temperatures. The percentage of linear shrinkage was calculated based on the initial and final sample lengths.
- (d) The point load strength was determined using a Point Load ELLE International (Gdańsk, Poland), following the standard test method [40].
- (e) The color variation with temperature was measured using an X-rite model SP 60 spectrophotometer (Grandville, MI, USA). The measurements were expressed in the CIE  $L^*a^*b^*$  scale, which is a standardized color scale using in colorimetry.
- (f) Dilatometric analysis was performed using an L75PT vertical dilatometer (DIL Dilatometer, TA Instruments, Hüllhorst, Germany), with test cylinders of 5 mm diameter and 10 mm length that were previously fired at  $1200^{\circ}$ ,  $1300^{\circ}$  and  $1400\text{ }^{\circ}\text{C}$ . The rate of firing was  $5\text{ }^{\circ}\text{C min}^{-1}$ , and the analysis was carried out in the temperature range of room temperature to  $1000\text{ }^{\circ}\text{C}$ .

### 3. Results

#### 3.1. Sampling Characterization

The alumina content varies between 34 and 40%, and silica values are generally high (ca. 40%), except in F2-Y (26%) (Table 1). The alkaline and alkaline earth elements/metals are quite low, except for sample FR-9 with 0.47% K<sub>2</sub>O. TiO<sub>2</sub> is present in all samples ranging from 1.7 to 2.7%. Iron ranges from 0.58% Fe<sub>2</sub>O<sub>3</sub> in sample F4-4 to nearly 16% in sample F2-Y. Considering the high alumina and low silica content, F4-4 and F2-Y are best suited for refractory “fireclay refractory” uses [8,41]. However, it is important to consider how high contents in silica or Fe oxides may affect mineralogical transformations at high temperatures.

**Table 1.** Major oxide composition (% wt.) by XRF.

Sample	SiO <sub>2</sub>	Al <sub>2</sub> O <sub>3</sub>	Fe <sub>2</sub> O <sub>3</sub>	MgO	CaO	Na <sub>2</sub> O	K <sub>2</sub> O	Ti <sub>2</sub> O <sub>3</sub>	P <sub>2</sub> O <sub>5</sub>	SO <sub>3</sub>	LOI
F2-X	41.11	37.34	4.60	0.11	0.14	N.D.	N.Q.	2.68	0.06	0.23	13.61
F2-Y	26.44	39.68	15.78	0.15	0.28	N.Q.	0.05	2.24	0.12	0.28	15.01
F4-4	43.72	38.91	0.58	0.16	0.17	0.04	0.05	1.95	0.05	N.D.	14.34
FR-9	39.59	33.90	9.32	0.35	0.56	N.D.	0.47	1.69	0.09	0.22	14.04
LoD	0.01	0.01	0.01	0.01	0.04	0.01	0.02	0.03	0.01	0.22	
LoQ	0.02	0.02	0.02	0.02	0.05	0.03	0.03	0.10	0.02	0.23	
ε <sub>r</sub>	0.012	0.020	0.058	0.007	0.047	0.038	0.028	0.061	0.025	0.063	0.01

Note: LOI—Loss on Ignition; LoD—Detection Limit; LoQ—Quantification Limit; N.D.—Not Detected; N.Q.—Not Quantified; ε<sub>r</sub>—Relative Error.

The mineralogical composition agrees with the chemical data, as verified by rational mineralogical analysis [42]. The bauxite materials are composed of kaolinite (with halloysite in FR-9) and traces of anatase and rutile (Table 2). The hematite content is variable, with a significant amount (16%) found in F2-Y. This sample also contains aluminum-rich phases such as gibbsite and boehmite.

**Table 2.** Mineralogical composition of the raw materials (whole sample and <2 μm fraction).

Samples	Whole Sample							<2 μm Fraction		
	Phy	Hm	Ant	Rt	Gbs	Bhm	I	Kaol	H	Chl
F2-X	93	tr	tr	tr	-	-	-	100	-	tr
F2-Y	55	16	tr	tr	12	12	-	100	-	-
F4-4	100	-	tr	tr	-	-	-	100	-	-
FR-9	95	5	tr	-	-	-	tr	77	17	tr

Note: tr—Trace (<5%); Phy—Phyllosilicates; Hm—Hematite; Ant—Anatase, Rt—Rutile; Gbs—Gibbsite; Bhm—Boehmite; I—Illite; Kaol—Kaolinite; H—Halloysite; Chl—Chlorite.

The results obtained by DTA showed the decomposition of gibbsite and its partial transformation to boehmite and alumina at ca. 310 °C and 445 °C, consistent with previous studies [43–48]. The dehydroxylation of kaolinite occurred about 560 °C, and the primary mullite crystallization was observed at 950 °C (Figure 3).

The degree of structural order of kaolinite, as determined by the AGFI index [37], showed the following sequence: F2-Y > F2-X > F4-4 > FR-9, with the last sample showing the presence of halloysite (Table 3). Similar results were obtained using the index of Bramao [38], except for sample FR-9, which showed a high structural order from low to high defect kaolinite. The structural order of kaolinite is a very interesting property in raw materials used for refractory applications, as it is directly proportional to the temperature of “secondary mullite” formation and is related to the total amount of mullite.

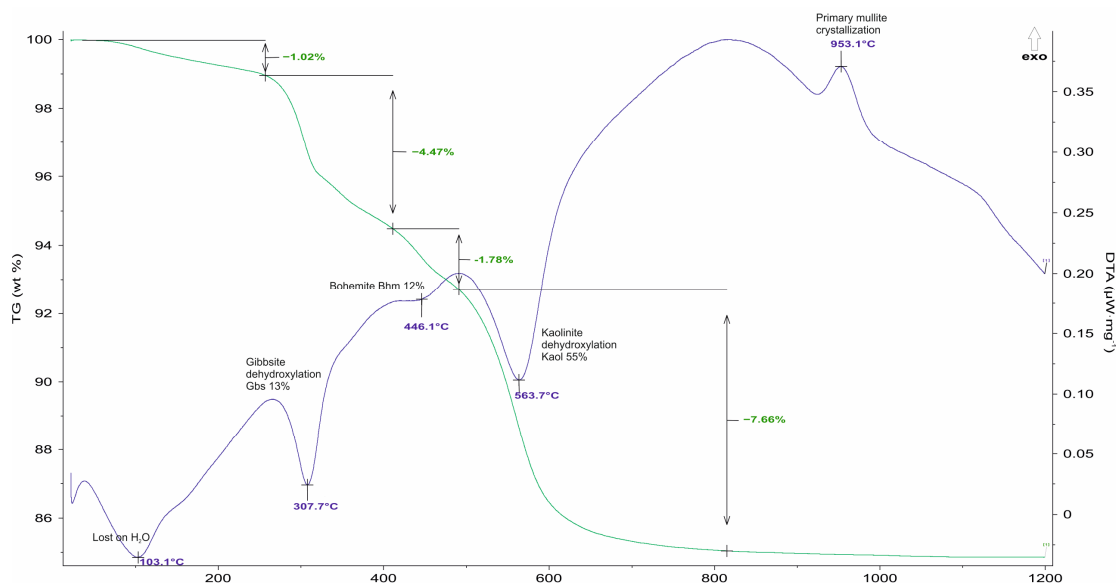


**Figure 3.** DTA/TG curves of sample F2-Y.

**Table 3.** Structural order in kaolinite by XRD (AGFI) and DTA (Bramao index).

Sample		AGFI	Bramao Index
F2-X	Medium defect kaolinite	1.17	1.563
F2-Y	Low defect kaolinite	1.55	1.864
F4-4	Medium defect kaolinite	1.18	1.589
FR-9	High defect kaolinite and halloysite	0.64	1.800

### 3.2. Ceramic Behavior

#### 3.2.1. Mineralogy at High Temperature

During the firing treatment, the kaolin minerals, anatase, boehmite and gibbsite were destroyed, while mullite and cristobalite crystallized, as shown in Figure 4. Rutile and hematite remained stable up to 1450 °C. In F2-Y, corundum, magnetite and ilmenite were formed starting from 1200 °C. The content in kaolinite, gibbsite and boehmite, as determined by XRD, was consistent with that established by TG analysis.

The content of mullite (reflections 210 and 110) increased with temperature in all samples (Figure 5). The relative percentage of mullite decreased in the order F2-Y > FR-9 ~ F2-X > F4-4, which does not entirely agree with alumina content. Cristobalite showed the highest relative percentage in samples F4-4 and F2-X, which is consistent with their silica content (Table 1). In those samples, cristobalite increased with temperature and remained in higher concentrations than mullite. On the contrary, in samples F2-Y and FR-9, cristobalite decreased with temperature, probably due to an increase in the silica amorphous phase up to 1450 °C caused by the dissolution of cristobalite [49].

#### 3.2.2. Textural Effects

Figure 6 displays the observation made using a tunnel heating microscope, showing the behavior of the specimens during firing at temperatures above 1000 °C. The results indicate that firing at temperatures above 1000 °C leads to contraction, likely due to an increase in the vitreous (glassy) phase. Likewise, this contraction can be also attributed to the solid-state sintering of kaolinite (and halloysite), leading to the subsequent neo-formation of mullite and cristobalite phases [50,51]. This contraction was observed to persist up to the final temperature of 1500 °C in the experiment. The most significant contraction of the specimens occurred between the temperature range of 1000–1200 °C. This information provides insight into the physical changes and behavior of the specimens during the firing process, particularly about their dimensional changes.

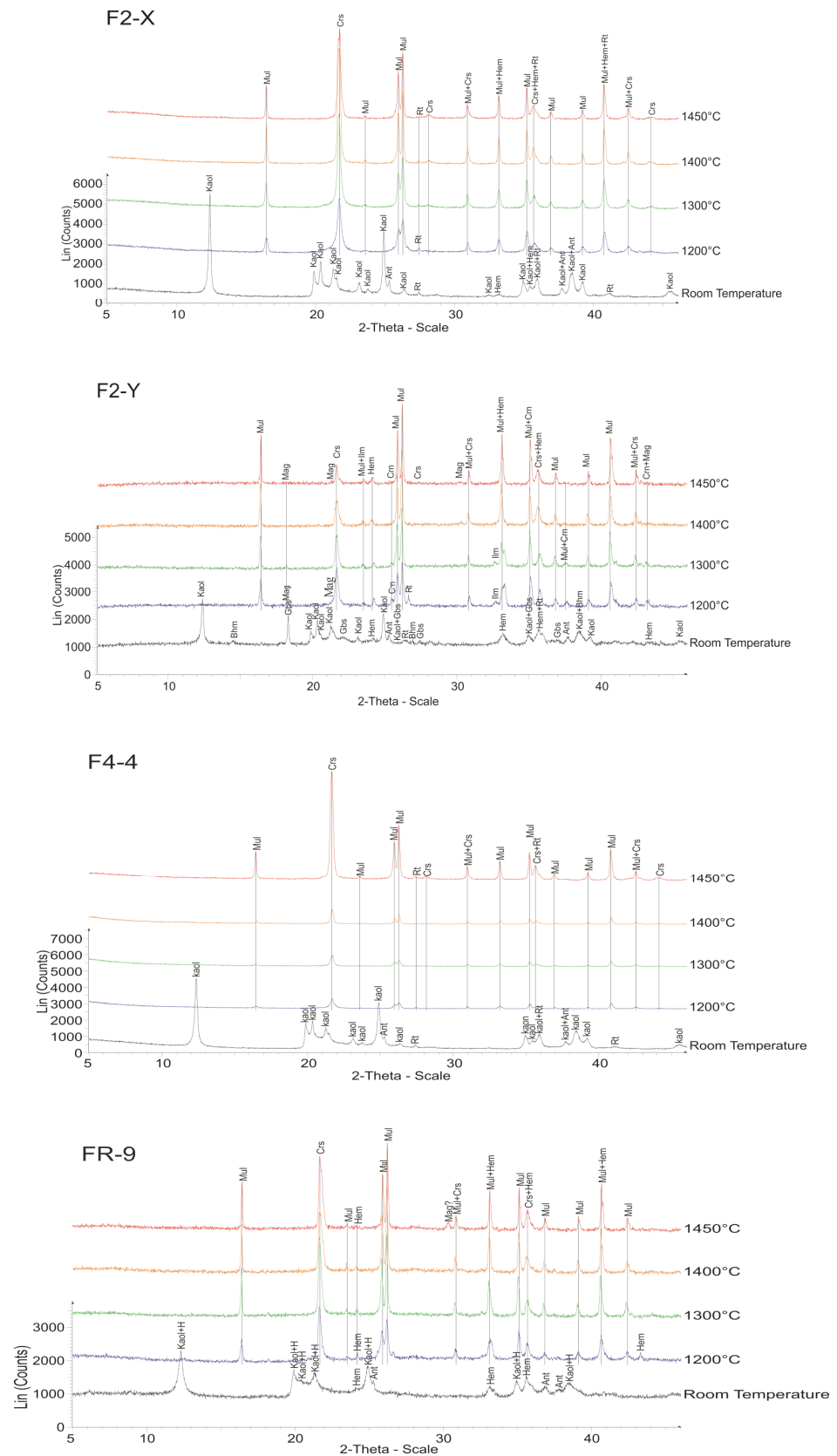


**Figure 4.** Comparison between XRD pattern of raw and fired samples (diffraction patterns have been offset along the Y-axis). Kaol: kaolinite, Kaol+H: kaolinite + halloysite, Ant: anatase, Rt: rutile, hem: hematite, Gbs: gibbsite, Bhm: boehmite, Mul: mullite, Crs: cristobalite, Crn: corundum, Ilm: Ilmenite, and Mag: magnetite.

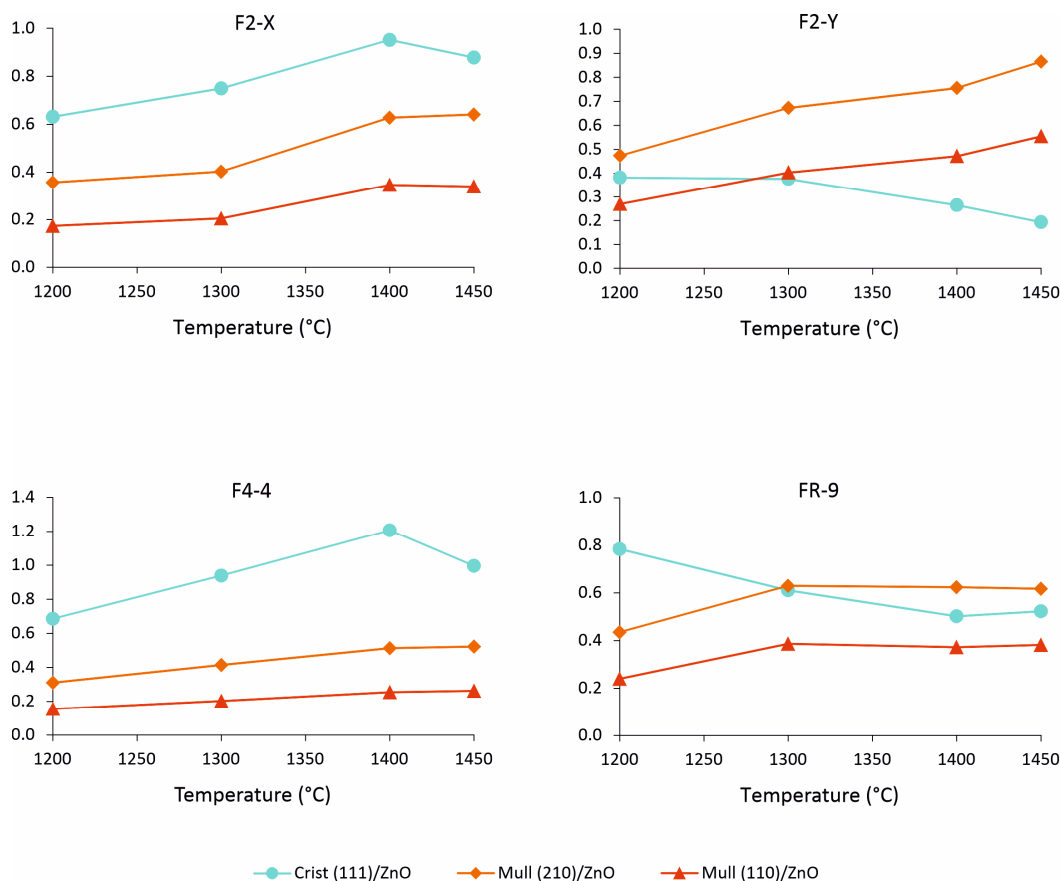


**Figure 5.** Crystalline phase (cristobalite and mullite) evolution with temperature (1200 to 1450 °C) as determined by XRD using zincite as internal standard (Sigma Aldrich, Steinheim, Germany).

In the case of sample F2-Y, the observations made using a tunnel heating microscope reveal an interesting phenomenon between 1300 and 1400 °C. In addition to the contraction, there is a diffusion of gases toward the surface, causing the expulsion of particles (Figure 6, F2-Y at 1300–1400 °C). This phenomenon is attributed to the behavior of iron oxide, which undergoes changes during firing in an oxidation environment. At temperatures up to approximately 1200 °C, iron oxide remains as  $\text{Fe}_2\text{O}_3$ , but it is then thermally reduced to  $\text{Fe}_3\text{O}_4$  on its way to becoming FeO. The complex iron oxide molecule is unable to maintain its state at these high temperatures, resulting in the release of an oxygen atom that bubbles to the surface of the hot glaze, carrying some iron with it. When oxygen reaches the surface, it releases the iron while leaving the glaze, creating spots with higher concentrations of iron oxide (Figure 6, F2-Y at 1300–1400 °C). With further heating, these spots begin to melt and run down the pot, resulting in a distinctive “hare’s fur” effect [52]. This phenomenon provides insight into the dynamic behavior of the samples during firing and the resulting effects on the surface appearance and composition of the glaze.

Based on the findings of this study, it appears that the melting point was not reached in F2-Y as expected, despite its high iron content [53]. This could be due to the incomplete reduction of ferric oxides ( $\text{Fe}_2\text{O}_3$ ) to ferrous oxide (FeO) during the firing, as evidence by the presence of magnetite ( $\text{Fe}_3\text{O}_4$ ) up to 1450 °C (Figure 4). The relatively low  $\text{SiO}_2$  content in F2-Y may not favor the reaction between the complex iron oxide molecule and silica at those temperatures, which would typically result in the formation of  $\text{FeSiO}_3$  and a decrease in the melting temperature of the glaze. This incomplete reduction of ferric oxide and the presence of magnetite may contribute to the observed behavior of F2-Y during firing and its failure to reach the expected melting point. This information offers an understanding of the intricate interactions among various components of the sample and their impact on the melting behavior during firing.

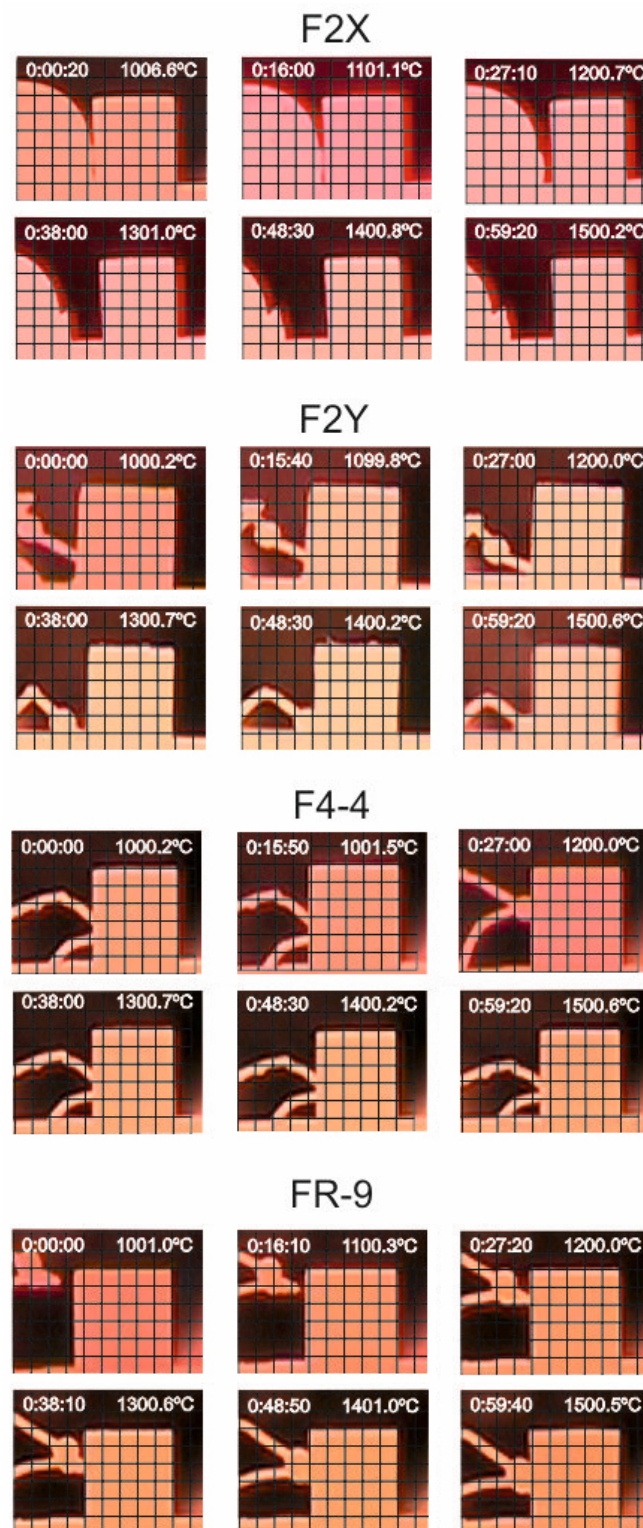


**Figure 6.** Textural evolution with temperature by tunnel heating microscopy.

### 3.2.3. Gresification Properties

All samples fired at 1100 °C exhibited a linear shrinkage of less than 10%, except for FR-9, which showed approximately 12% linear shrinkage (Figure 7). This higher linear shrinkage in FR-9 can be attributed to the increased formation of the liquid phase at this temperature, likely due to the presence of fluxing agents such as  $K_2O$ ,  $CaO$  and  $MgO$  (Table 1). The reduced open pores in FR-9 was caused by the densification of this material.

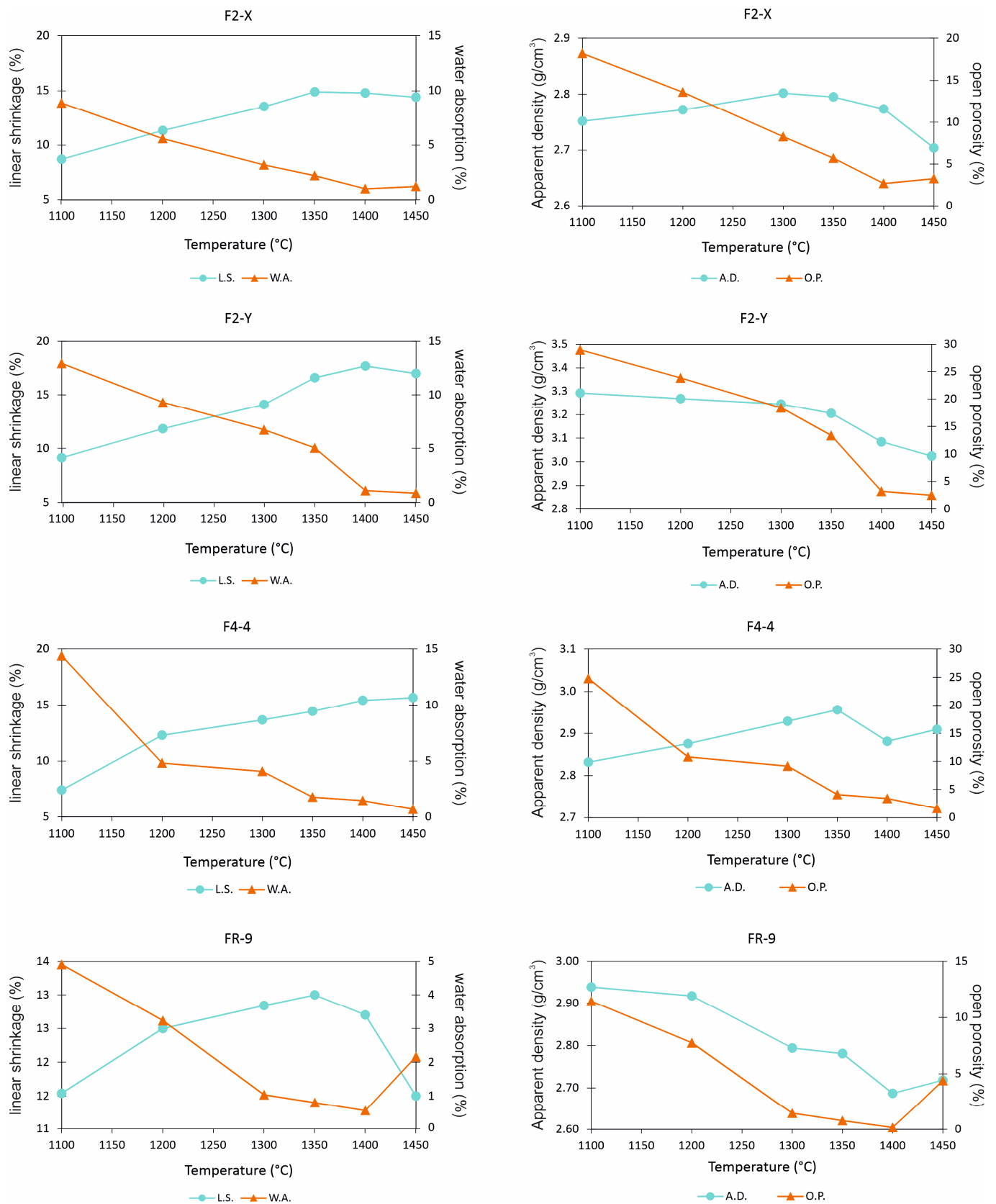


**Figure 7.** Influence of firing temperature on the sintering parameters: linear shrinkage (L.S.), water absorption (W.A.), apparent density (A.D.) and open porosity (O.P.).

The generalized decrease (until at least 1400 °C) in linear shrinkage is primarily attributed to the formation of mullite, glass and the quartz–cristobalite phase transformation, which result in pore closure [8,54]. Water absorption values of samples fired at 1450 °C were close to 0%, except for FR-9, which exhibited a sharp increase at 1400 °C. This increase probably is attributed to the formation of micro-cracks due to the presence of high alkaline earth elements and Fe oxides. Additionally, the linear shrinkage of FR-9 showed a sharp change after 1400 °C, indicating significant changes in its sintering behavior at higher temperatures.

The apparent density of F2-Y is notably high, with a value exceeding 3 g/cm<sup>3</sup>, which is likely attributed to its high mullite/cristobalite ratio. The open porosity of F2-Y decreased as a result of the expansion associated with the polymorphic transformations of quartz–cristobalite and the formation of glass that occur on firing at high temperatures [55]. This reduction in porosity leads to a decrease in volume while simultaneously improving the mechanical properties of the material.

Hence, based on the gresification diagrams, it can be concluded that the optimum firing range for all samples is 1400–1450 °C, except for FR-9, which should be fired a slightly lower temperature between 1300–1400 °C due to the formation of micro-cracks.

The color evolution with the temperature, as depicted in Figure 8, reveals that the F2-X and F4-4 samples exhibit a whitish coloration up to 1400 °C, characterized by the high value of L\* and the low values of a\* and b\*. Subsequently, F2-X acquires yellowish and reddish hues beyond 1400 °C. On the other hand, the F4-4 sample maintains an unchanged tonality across the entire temperature range. In contrast, the F2-Y and FR-9 samples display a reddish coloration initially, which transitions to dark gray starting from 1350 °C, as evidence by the decrease in a\* and b\* parameters.

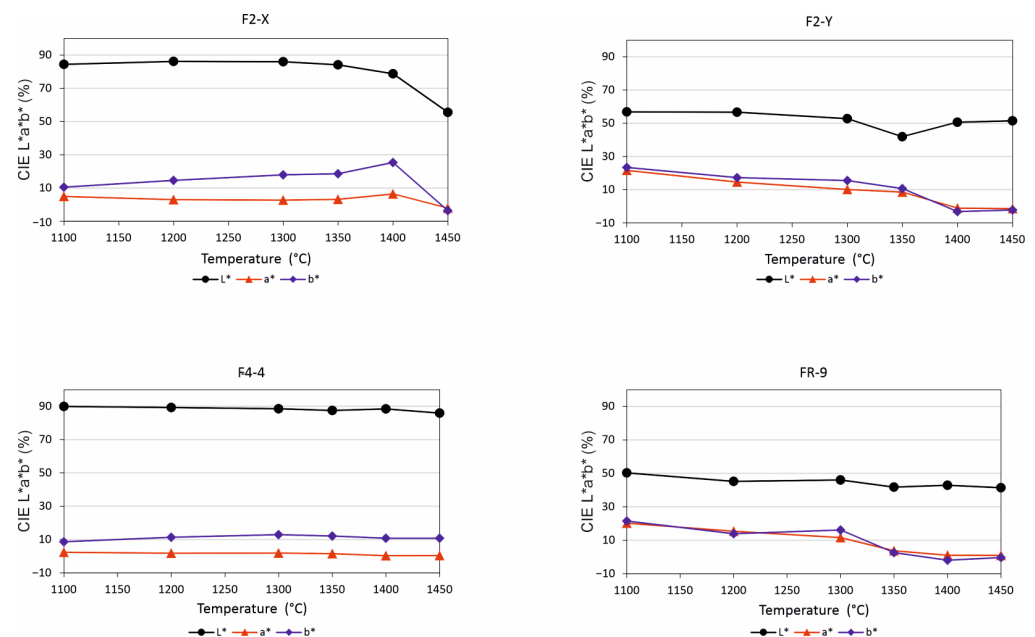


**Figure 8.** Color variation during heating.

These color changes during heating can be attributed to various factors, including the formation of different phases, changes in the composition and crystal structure of the samples, and the occurrence of chemical reactions, which can influence the absorption, reflection and transmission of light, resulting in different color appearances. The color changes observed in the samples provide valuable information about their thermal behavior and can be used to understand the firing process and optimize the firing conditions for desired color outcomes in ceramic materials.

### 3.2.4. Dilatometric Behavior

Dilatometric tests (as shown in Figure 9) conducted on samples previously fired at 1200°, 1300° and 1400 °C revealed a pronounced expansion between 100 and 200 °C, except in F2-Y. This expansion, resulting in a volume change up to 3%, is attributed to the presence of cristobalite, which undergoes  $\alpha \leftrightarrow \beta$  transformation between 160° and 275 °C. This high expansion/shrinkage coefficient of cristobalite, which forms from 1200 °C due to the silica content, can reduce the number of heating cycles required. Subsequently, after the sharp expansion at low temperatures, the dilatation increases linearly from 200 °C but with a lower gradient, as expected. However, in the case of the F2-Y sample, which contains the lowest proportion of cristobalite, this change in dilatation was not significant and was not detected in the cylinder fired at 1400 °C. This indicates that the presence of cristobalite has a pronounced influence on the dilatometric behavior of the samples, particularly at lower temperatures.

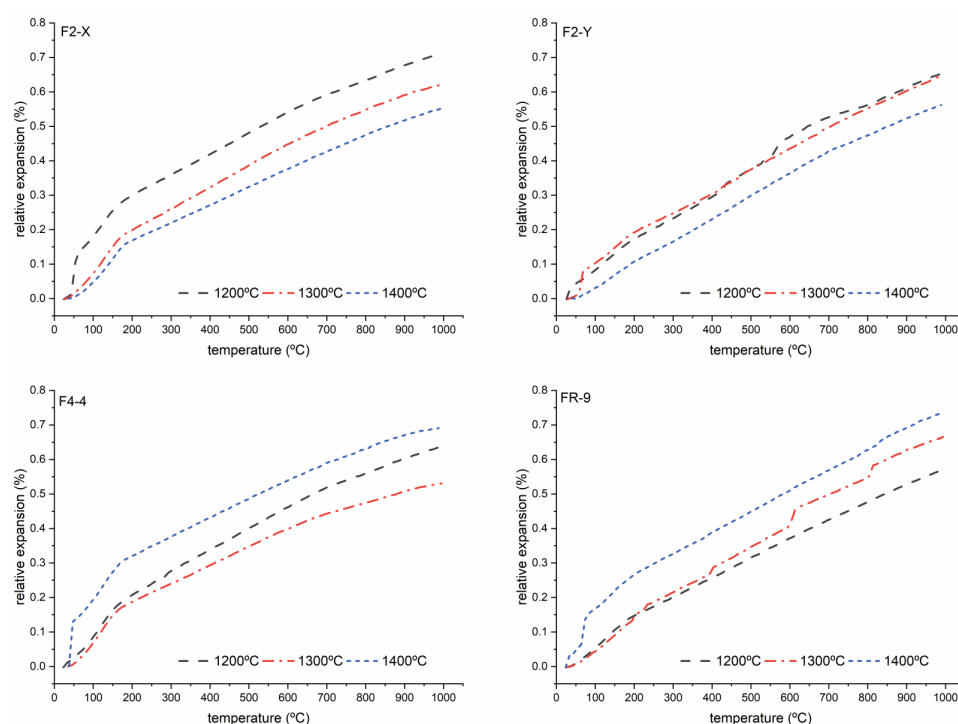


**Figure 9.** Thermal expansion curves over the range from room temperature (RT) to 1000 °C.

In contrast, the samples F4-4 and FR-9 exhibited higher dilatation in the cylinders fired at higher temperatures, probably due to the high proportion of cristobalite relative to mullite, which is consistent with their elevated silica and reduced alumina content. Conversely, in samples F2-X and F2-Y, the dilatation was lower in the cylinders fired at higher temperatures.

Hence, based on the results obtained, F2-Y was deemed to be the most suitable sample for use as a refractory material due to its higher mullite/cristobalite ratio, which reduces the dilation and shrinkage phenomena and allows for a higher number of life cycles. On the other hand, F4-4 presented the greatest dilatometric variation, particularly at 1400 °C, due to its high content of cristobalite. However, in the range of 1200–1300 °C, F4-4 showed a lower percentage of cristobalite, while mullite remained comparable to that at higher temperatures. Consequently, the dilation value was lower, implying that a firing temperature in this range may be recommended for F4-4 to minimize dilation-related issues.

### 3.2.5. Mechanical Strength

The point load strength of the samples increased, while the water absorption decreased, as shown in Figure 10. This increase in strength is likely attributed to the formation of a mullite and vitreous phase, as opposed to cristobalite. However, a decrease in the strength was observed in the temperature range of 1350–1400 °C, which could be due to the formation of micro-cracks. As a result, the water absorption remained stable or even increased in this temperature interval.

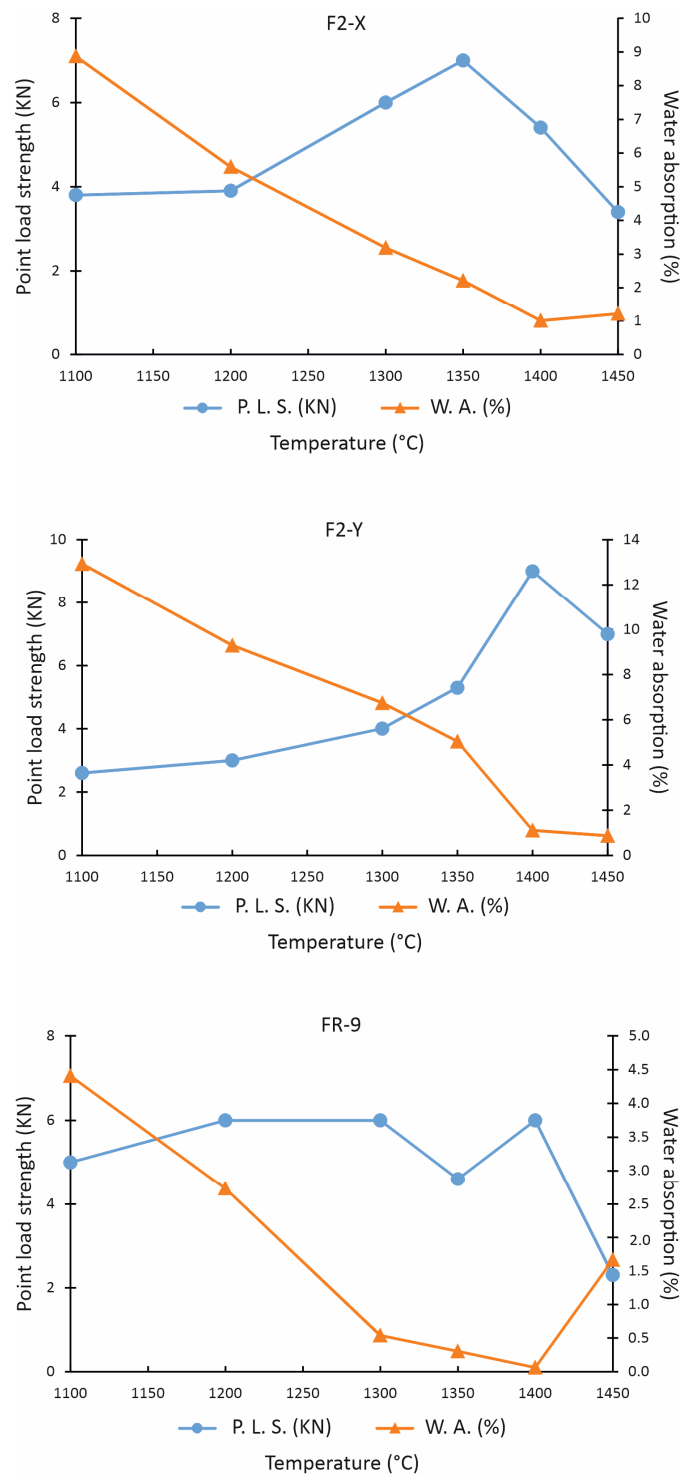


Figure 10. Variations in the point load strength and water absorption with temperature.

#### 4. Discussion

The use of bauxites and fireclays as refractory materials depends primarily on their alumina and silica content, but other impurities such as alkaline and alkaline earth elements, iron oxides and titanium can also affect the refractory properties [18,19]. In our case, according to the alumina content, samples F4-4 and F2Y are well suited for refractory uses. However, the high content of silica may reduce the refractory properties and the quality of the final product. As a result, sample F4-4, with 43.7% SiO<sub>2</sub>, exhibited a low mullite/cristobalite proportion, which reduces its refractory properties. Other studies have shown that iron oxy-hydroxides can deteriorate the refractory properties, cause deformation and decrease the melting point [16,18]. On the contrary, the high content of iron in sample F2-Y did not significantly affect its properties, as the reduction of hematite to magnetite started from 1300 °C, and hematite remained stable up to 1500 °C. However, iron content did impact the color of F2-Y and FR-9, which changed between 1300 and 1350 °C. In terms of alkali content, the relatively high K<sub>2</sub>O content in sample FR-9 (0.47%) appears to have affected its linear shrinkage at 1200 °C and the formation of micro-cracks at 1400 °C. It is known that even low concentrations of alkaline components can decrease the melting temperature [20–22].

In Al-rich systems, the refractory properties are highly dependent on the content of mullite [8]. The results of this study have shown that, more than the total content, the proportion of mullite with respect to cristobalite was a key factor. The transformation of cristobalite to amorphous silica with increasing temperatures [49] and the crystallization of mullite were observed to reduce the open porosity and volume, while increasing the mechanical properties of the studied samples [8,54]. Moreover, the mullite/cristobalite proportion also affected the dilatometric properties of the bauxite samples, reducing the dilation/shrinkage phenomena and increasing the number of life cycles.

According to the gresification diagrams, the optimal firing temperature for the samples studied was found to be around 1400–1450 °C. However, it was observed that the mechanical properties can deteriorate from 1400 °C onwards, likely due to the formation of micro-cracks. This effect was particularly notable in sample FR-9, which may require a lower firing temperature of 1300–1400 °C to avoid micro-crack formation. In the case of sample F4-4, the high content of cristobalite caused significant dilatometric variation, which may reduce the number of life cycles. Therefore, the optimal firing temperature for F4-4 may be around 1200–1300 °C to minimize dilatometric variation. On the other hand, sample F2-Y, with a high mullite/cristobalite proportion, exhibited better refractory properties, with reduced dilation/shrinkage phenomena and an increased number of life cycles. However, due to its iron content, the color of F2-Y can change between 1300 and 1350 °C. Therefore, reducing the iron content in samples F2-Y and FR-9 could potentially improve their ceramic properties.

#### 5. Conclusions

In conclusion, the refractory properties of bauxitic materials are influenced by their chemical and mineralogical composition. A silica content higher than 40% can reduce the refractory properties and the quality of the final product. Other components, such as iron oxy-hydroxides, alkali and alkaline earth elements increased the linear shrinkage and caused the formation of micro-cracks, especially at 1400 °C, as observed in sample FR-9 with a low content in alumina.

Sample F2-Y, with a high proportion of alumina and iron and relatively low silica content, exhibited good refractory behavior with high mechanical strength and a high number of life cycles, thanks to its low cristobalite content. However, the color change at 1300–1350 °C and the high iron content could be improved through techniques such as magnetic separation or chemical leaching.

FR-9 showed promising refractory behavior due to the high amount of mullite produced at high temperatures, but its high alkaline earth and Fe-oxide content lowered the optimal firing temperature to 1300–1400 °C.

On the other hand, F2-X and F4-4 were found to have relatively high cristobalite content and low mechanical resistance, limiting their suitability for refractory applications. They may be used as refractories fired at 1200° or 1300 °C, but with a moderate number of heating cycles.

In summary, the mullite/cristobalite proportion, silica content, iron content and other chemical components play critical roles in determining the refractory properties of bauxitic materials, and optimizing the firing temperature and employing techniques such as the separation or reduction of certain components can potentially improve their refractory behavior for various industrial applications. Further research and optimization of processing conditions are recommended to fully understand and utilize the refractory properties of these materials.

**Author Contributions:** Conceptualization, P.A. and D.M.; methodology, I.G., A.M. and D.M.; validation, P.C., A.R.-B., C.B.-B. and J.D.; formal analysis, A.M. and D.M.; investigation, I.G.; resources, P.A.; data curation, D.M. and A.M.; writing—original draft preparation, A.M. and D.M.; writing—review and editing, D.M.; supervision, D.M. and A.M.; funding acquisition, P.A. All authors have read and agreed to the published version of the manuscript.

**Funding:** This research was supported by funding from the Spanish Ministerio de Educación y Ciencia (CGL2013-46169-C2-2-P) and the contract of Domingo Martín granted by the V Plan Propio de Investigación de la Universidad de Sevilla (VPPI-5-2015).

**Data Availability Statement:** Data are contained within the article.

**Acknowledgments:** Analytical measurements were conducted at the “Centro de Investigación, Tecnología e Innovación, CITIUS” of Sevilla University.

**Conflicts of Interest:** The authors declare no conflicts of interest in the material discussed in this article.

## References

1. Criado Herrero, E.; Enrique Navarro, J.E. Tendencias Generales En La Industria Española de Cerámica y Refractarios. *Bol. Soc. Esp. Ceram. Vidr.* **1994**, *33*, 125–134.
2. Jenkins, B.; Mullinger, P. *Industrial and Process Furnaces: Principles, Design and Operation*; Butterworth-Heinemann: Oxford, UK, 2022; ISBN 0323984916.
3. Walker, H. Classes of Refractories. In *Handbook of Refractory Practice*; Harbison Walker Refractories Company: Moon Township, PA, USA, 2005; pp. 9–31.
4. Sarpoolaky, H.; Ahari, K.G.; Lee, W.E. Influence of in Situ Phase Formation on Microstructural Evolution and Properties of Castable Refractories. *Ceram. Int.* **2002**, *28*, 487–493. [[CrossRef](#)]
5. Mergen, A. Production of Sintered High Alumina Refractories from Turkish Bauxite Ore. *Adv. Appl. Ceram.* **2004**, *103*, 42–46. [[CrossRef](#)]
6. Karadeniz, E.; Gurcan, C.; Ozgen, S.; Aydin, S. Properties of Alumina Based Low-Cement Self Flowing Castable Refractories. *J. Eur. Ceram. Soc.* **2007**, *27*, 1849–1853. [[CrossRef](#)]
7. Gonçalves, J.P.; Tavares, L.M.; Toledo Filho, R.D.; Fairbairn, E.M.R. Performance Evaluation of Cement Mortars Modified with Metakaolin or Ground Brick. *Constr. Build Mater.* **2009**, *23*, 1971–1979. [[CrossRef](#)]
8. Caniglia, S.; Barna, G.L. *Handbook of Industrial Refractories Technology: Principles, Types, Properties and Applications*; William Andrew: Norwich, NY, USA, 1992; ISBN 0815517564.
9. Mutakyahwa, M.K.D.; Ikingura, J.R.; Mruma, A.H. Geology and Geochemistry of Bauxite Deposits in Lushoto District, Usambara Mountains, Tanzania. *J. Afr. Earth Sci.* **2003**, *36*, 357–369. [[CrossRef](#)]
10. Calagari, A.A.; Abedini, A. Geochemical Investigations on Permo-Triassic Bauxite Horizon at Kanisheeteh, East of Bukan, West-Azarbaidjan, Iran. *J. Geochem. Explor.* **2007**, *94*, 1–18. [[CrossRef](#)]
11. Dill, H.G. Residual Clay Deposits on Basement Rocks: The Impact of Climate and the Geological Setting on Supergene Argillitization in the Bohemian Massif (Central Europe) and across the Globe. *Earth Sci. Rev.* **2017**, *165*, 1–58. [[CrossRef](#)]
12. Bárdossy, G.; Aleva, G.J.J. *Lateritic Bauxites*; Akadémiai Kiadó: Budapest, Hungary, 1990; ISBN 9630554917.
13. Brindley, G.W.; Maroney, D.M. High-Temperature Reactions of Clay Mineral Mixtures and Their Ceramic Properties: II, Reactions of Kaolinite-Mica-Quartz Mixtures Compared with the  $K_2O-Al_2O_3-SiO_2$  Equilibrium Diagram. *J. Am. Ceram. Soc.* **1960**, *43*, 511–516. [[CrossRef](#)]
14. Brindley, G.W.; Nakahira, M. The Kaolinite-Mullite Reaction Series: II, Metakaolin. *J. Am. Ceram. Soc.* **1959**, *42*, 314–318. [[CrossRef](#)]
15. Brindley, G.W.; Nakahira, M. The Kaolinite-Mullite Reaction Series: III, The High-Temperature Phases. *J. Am. Ceram. Soc.* **1959**, *42*, 319–324. [[CrossRef](#)]

16. De Aquino, T.F.; Riella, H.G.; Bernardin, A.M. Mineralogical and Physical-Chemical Characterization of a Bauxite Ore from Lages, Santa Catarina, Brazil, for Refractory Production. *Miner. Process. Extr. Metall. Rev.* **2011**, *32*, 137–149. [CrossRef]
17. Pruet, R.J. Kaolin Deposits and Their Uses: Northern Brazil and Georgia, USA. *Appl. Clay Sci.* **2016**, *131*, 3–13. [CrossRef]
18. Andji, J.Y.Y.; Toure, A.A.; Kra, G.; Jumas, J.C.; Yvon, J.; Blanchart, P. Iron Role on Mechanical Properties of Ceramics with Clays from Ivory Coast. *Ceram Int.* **2009**, *35*, 571–577. [CrossRef]
19. Aksaf, I.A.; Pask, J.A. Stable and Metastable Equilibria in the System  $\text{SiO}_2\text{-Al}_2\text{O}_3$ . *J. Am. Ceram. Soc.* **1975**, *58*, 507–512. [CrossRef]
20. Wang, Y.; Hu, Y.; He, P.; Gu, G. Reverse Flotation for Removal of Silicates from Diasporic-Bauxite. *Min. Eng* **2004**, *17*, 63–68. [CrossRef]
21. Hyun, J.; Endoh, S.; Masuda, K.; Shin, H.; Ohya, H. Reduction of Chlorine in Bauxite Residue by Fine Particle Separation. *Int. J. Min. Process* **2005**, *76*, 13–20. [CrossRef]
22. Jenkins, D.H.; Sinha, H.N. Leaching Kinetics of Bauxite in Hydrochloric Acid. *Miner. Process. Extr. Metall. Rev.* **1995**, *15*, 143. [CrossRef]
23. Gualtieri, A.; Bellotto, M.; Gualtieri, A. Modelling the Structure of the Metastable Phases in the Reaction Sequence Kaolinite-Mullite by X-Ray Scattering Experiments. *Phys. Chem. Miner.* **1998**, *25*, 442–452. [CrossRef]
24. Fielitz, P.; Borchardt, G.; Schmücker, M.; Schneider, H. Aluminium Grain Boundary Diffusion in Polycrystalline Mullite Ceramics. *Phys. Chem. Min.* **2007**, *34*, 431–436. [CrossRef]
25. Yuste, A.; Bauluz, B.; Mayayo, M.J. Genesis and Mineral Transformations in Lower Cretaceous Karst Bauxites (NE Spain): Climatic Influence and Superimposed Processes. *Geol. J.* **2015**, *50*, 839–857. [CrossRef]
26. Laita, E.; Bauluz, B.; Mayayo, M.J.; Yuste, A. Mineral and Textural Transformations in Mixtures of Al-Rich and Al-K-Rich Clays with Firing: Refractory Potential of the Fired Products. *Ceram Int.* **2021**, *47*, 14527–14539. [CrossRef]
27. Laita, E.; Yuste, A.; Badenas, B.; Bauluz, B.; Aurell, M. Weathering Events Recorded in Uppermost Hauterivian-Lower Barremian Clay-Dominated Continental Successions from the NW Iberian Range: Climatic vs. Tectonic Controls. *J. Iber. Geol* **2022**, *48*, 45–63. [CrossRef]
28. Ordóñez, S. Las Bauxitas Españolas Como Mena de Aluminio. *Fund. Juan March Madr.* **1977**, *33*, 64.
29. Gobierno de España. Ministerio Para la Transición Ecológica y el Reto Demográfico. *Estadísticas. España*. Available online: <https://www.miteco.gob.es/es/biodiversidad/estadisticas/> (accessed on 20 July 2023).
30. Galan, E.; Lopez-Aguayo, F.; De-Aza, S. Bauxitic Clays of NE Teruel (Spain). In Proceedings of the 7th Conference of Clay Minerals and Petrology; 1977; pp. 487–497.
31. Mojon, P.-O. Précisions Sur l'intervalle Valanginien-Barrémien de La Biozonation Des Charophytes Du Crétacé Inférieur Du Mestrazgo (Chaîne Ibérique Orientale, Espagne) et Sur La Biozonation Des Charophytes de l'intervalle Jurassique Supérieur-Crétacé de l'Europe Occidentale. *Geol. Alp.* **1996**, *72*, 61–99.
32. Huertos, E.G.; Vivaldi, J.L.M. Caolines Españoles: Parte I. Geología, Minerología y Génesis. *Bol. Soc. Esp. Ceram. Vidr.* **1973**, *12*, 79–98.
33. Martín-Pozas, J.M.; Galán, E.; Martín-Vivaldi, J.L. Il Giacimento Di Caolino Di Jove, Lugo, Spagna. In Proceedings of the I Congresso Nazionale; AIPEA Italia Pavia, Venezia-Faenza, Italy, 16–19 May 1971; pp. 89–109.
34. Schultz, L.G. Quantitative Interpretation of Mineralogical Composition from X-ray and Chemical Data for the Pierre Shale. *Geol. Surv. Prof. Pap* **1964**, *391*, 1–31.
35. Aparicio, P.; Márquez, M.G.; Galán, E.; Miras, A.; Caliani, J.C. Avances En La Determinación y Cuantificación de Halloysita En Caolines Mediante DRX. Aplicación al Caolín de Burela (Lugo). In Proceedings of the Jornadas Científicas de la Sociedad Española de Arcillas, Sevilla, Spain, 16 November 2007.
36. Aparicio, P.; Ferrell, R.E.; Galán, E. A New Kaolinite Crystallinity Index from Mathematical Modelling of XRD Data. In Proceedings of the Conference of the European Clay Group Association, Kraków, Poland, 5–9 September 1999; p. 57.
37. Aparicio, P.; Galán, E.; Ferrell, R.E. A New Kaolinite Order Index Based on XRD Profile Fitting. *Clay Min.* **2006**, *41*, 811–817. [CrossRef]
38. Bramaio, L.; Cady, J.G.; Hendricks, S.B.; Swerdlow, M. Criteria for the Characterization of Kaolinite, Halloysite, and a Related Mineral in Clays and Soils. *Soil Sci.* **1952**, *73*, 273–288. [CrossRef]
39. *ASTM C20-00(2022)*; Standard Test Methods for Apparent Porosity, Water Absorption, Apparent Specific Gravity, and Bulk Density of Burned Refractory Brick and Shapes by Boiling Water. ASTM International: West Conshohocken, PA, USA, 2022.
40. *ASTM D5731-08*; Standard Test Method for Determination of the Point Load Strength Index of Rock and Application to Rock Strength Classifications. ASTM International: West Conshohocken, PA, USA, 2008; Volume 22.
41. Wang, S.; Gainey, L.; Mackinnon, I.D.R.; Xi, Y. High-and Low-Defect Kaolinite for Brick Making: Comparisons of Technological Properties, Phase Evolution and Microstructure. *Constr. Build Mater.* **2023**, *366*, 130250. [CrossRef]
42. Coelho, C.; Roqueiro, N.; Hotza, D. Rational Mineralogical Analysis of Ceramics. *Mater. Lett.* **2002**, *52*, 394–398. [CrossRef]
43. Brown, J.F.; Clark, D.; Elliott, W.W. The Thermal Decomposition of the Alumina Trihydrate, Gibbsite. *J. Chem. Soc.* **1953**, 84–88. [CrossRef]
44. Castaldi, P.; Santona, L.; Enzo, S. XRD, FTIR, and Thermal Analysis of Bauxite Ore-Processing Waste (Red Mud) Exchanged with Heavy Metals. *Clays Clay Min.* **2008**, *56*, 461–469. [CrossRef]
45. Atasoy, A. The Comparison of the Bayer Process Wastes on the Base of Chemical and Physical Properties. *J. Therm. Anal. Calorim.* **2007**, *90*, 153–158. [CrossRef]

46. Jokanovic, V.; Jokanovic, B.; Markovic-Todorovic, B.; Markovic, Z. Synthesis and Characterization of Hydrothermally Obtained Colloidal Pseudoboehmite/Boehmite. *J. Optoelectron. Adv. Mater.* **2009**, *11*, 164.
47. Kozerzhets, I.V.; Panasyuk, G.P.; Semenov, E.A.; Avdeeva, V.V.; Danchevskaya, M.N.; Simonenko, N.P.; Vasiliev, M.G.; Lyubov'O, K.; Ivakin, Y.D. Recrystallization of Nanosized Boehmite in an Aqueous Medium. *Powder. Technol.* **2023**, *413*, 118030. [[CrossRef](#)]
48. Zanganeh, S.; Kajbafvala, A.; Zanganeh, N.; Mohajerani, M.S.; Lak, A.; Bayati, M.R.; Zargar, H.R.; Sadrnezhad, S.K. Self-Assembly of Boehmite Nanopetals to Form 3D High Surface Area Nanoarchitectures. *Appl. Phys. A* **2010**, *99*, 317–321. [[CrossRef](#)]
49. Kolli, M.; Hamidouche, M.; Fantozzi, G.; Chevalier, J. Elaboration and Characterization of a Refractory Based on Algerian Kaolin. *Ceram. Int.* **2007**, *33*, 1435–1443. [[CrossRef](#)]
50. Gualtieri, A.F. Thermal Behavior of the Raw Materials Forming Porcelain Stoneware Mixtures by Combined Optical and in Situ X-ray Dilatometry. *J. Am. Ceram. Soc.* **2007**, *90*, 1222–1231. [[CrossRef](#)]
51. Wang, S.; Gainey, L.; Mackinnon, I.D.R.; Allen, C.; Gu, Y.; Xi, Y. Thermal Behaviors of Clay Minerals as Key Components and Additives for Fired Brick Properties: A Review. *J. Build. Eng.* **2022**, *66*, 105802. [[CrossRef](#)]
52. Britt, J. *The Complete Guide to High-Fire Glazes*; Sterling Publishing Company, Inc.: New York, NY, USA, 2007; ISBN 1600592163.
53. Bleining, A.; Brown, G.H. *The Testing of Clay Refractories, with Special Reference to Their Load Carrying Capacity at Furnace Temperatures*; US Government Printing Office: Washington, DC, USA, 1912.
54. Chesters, J.H. *Refractories—Production and Properties*; Iron and Steel Institute: London, UK, 1973; 553p.
55. Kingery, W.D.; Bowen, H.K.; Uhlmann, D.R. *Introduction to Ceramics*; John Wiley & Sons: Hoboken, NJ, USA, 1976; Volume 17, ISBN 0471478601.

**Disclaimer/Publisher's Note:** The statements, opinions and data contained in all publications are solely those of the individual author(s) and contributor(s) and not of MDPI and/or the editor(s). MDPI and/or the editor(s) disclaim responsibility for any injury to people or property resulting from any ideas, methods, instructions or products referred to in the content.